Nano Research

ISSN 1998-0124 CN 11-5974/O4
https://doi.org/10.26599/NR.2026.94909317

Research Article

Hydrothermally grown ZnO nanoarrays on phase-change core-shell fibers for solar heat-load reduction and thermal buffering

Chang Zhang[1,2], Yunfei Rao[1,2](✉), Furong Liu[1,2], Shengjie Dai[1,2], Chen Zhang[3], Fei Sun[1,2](✉), Feichao Zhu[1,2], Bin Yu[1,2](✉)

[1] State Key Laboratory of Bio-Based Fiber Materials, Zhejiang Sci-Tech University, Hangzhou 310018, China

[2] College of Textile Science and Engineering, Zhejiang Sci-Tech University, Hangzhou 310018, China

[3] Shanghai Science and Technology Exchange Center (SSTEC), Shanghai 200030, China

Nano Res., **Just Accepted Manuscript** • https://doi.org/10.26599/NR.2026.94909317

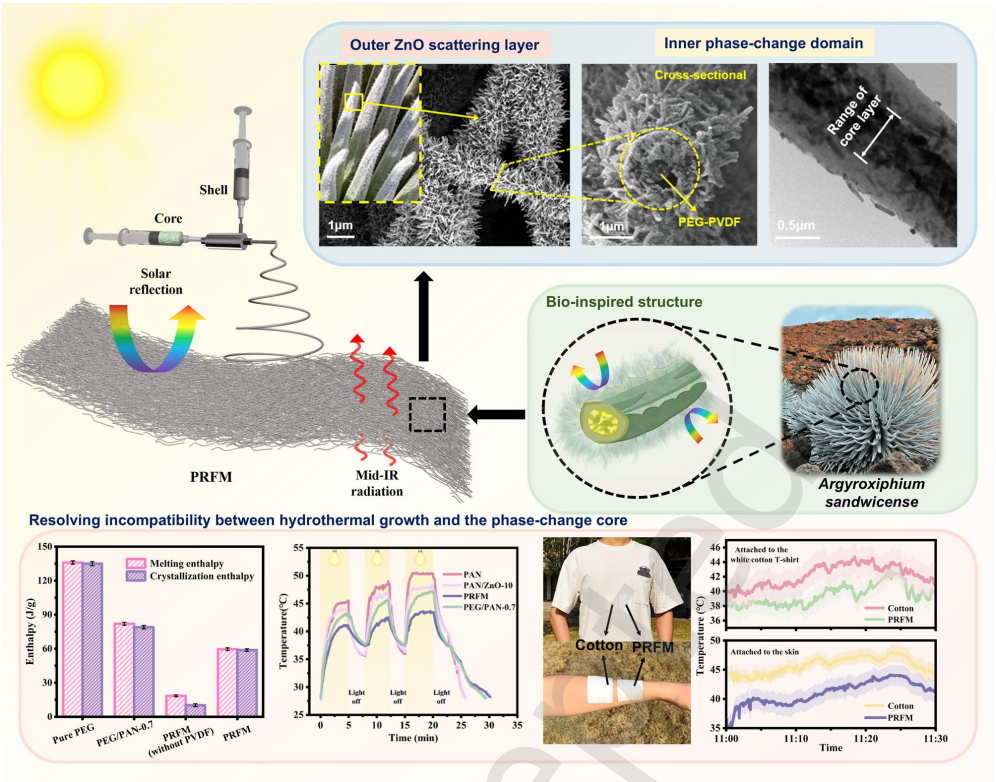
https://www.sciopen.com/journal/1998-0124 on Nov. 10, 2026

© The Authors(s)

Just Accepted

This is a "Just Accepted" manuscript, which has been examined by the peer-review process and has been accepted for publication. A "Just Accepted" manuscript is published online shortly after its acceptance,which is prior to technical editing and formatting and author proofing. Tsinghua University Press (TUP) provides "Just Accepted" as an optional and free service which allows authors to make their results available to the research community as soon as possible after acceptance. After a manuscript has been technically edited and formatted, and the page proofs have been corrected, it will be removed from the "Just Accepted" web site and published officially with volume and article number (e.g., *Nano Research*, **2025**, *18*, 94906990). Please note that technical editing may introduce minor changes to the manuscript text and/or graphics which may affect the content, and all legal disclaimers that apply to the journal pertain. In no event shall TUP be held responsible for errors or consequences arising from the use of any information contained in these "Just Accepted" manuscripts. To cite this anuscript please use its Digital Object Identifier (DOI®),which is identical for all formats of publication.

Just Accepted



To address the process incompatibility between the water- sensitive phase- change core layer and the in- situ hydrothermal growth, we propose a novel construction strategy that utilizes coaxial electrospinning and a PVDF hydrophobic shield to integrate an outer ZnO scattering layer and an inner PEG phase- change domain within a single fiber, achieving efficient synergistic regulation of daytime radiative cooling and thermal buffering.

Just Accepted

Research Article

Hydrothermally grown ZnO nanoarrays on phase-change core-shell fibers for solar heat-load reduction and thermal buffering

Chang Zhang [1,2], Yunfei Rao [1,2] ✉, Furong Liu [1,2], Shengjie Dai [1,2], Chen Zhang [3], Fei Sun [1,2] ✉, Feichao Zhu [1,2], Bin Yu [1,2] ✉

[1] State Key Laboratory of Bio-Based Fiber Materials, Zhejiang Sci-Tech University, Hangzhou 310018, China
[2] College of Textile Science and Engineering, Zhejiang Sci-Tech University, Hangzhou 310018, China
[3] Shanghai Science and Technology Exchange Center (SSTEC), Shanghai 200030, China

Received: 25 August 2026; **Revised: 31 October 2026**; **Accepted: 10 November 2026**

✉Address correspondence to Yunfei Rao, yunfei.rao@zstu.edu.cn; Fei Sun, sunfei_92@zstu.edu.cn; Bin Yu, yubin7712@163.com

Cite this article: *Nano Research*, 2027, 20, 94909317 https://doi.org/10.26599/NR.2026.94909317

Just Accepted

ABSTRACT: Integrating a phase-change core with hydrothermally grown optical nanostructures remains challenging because water-sensitive phase-change components may be lost or structurally damaged during aqueous mineralization. Inspired by the hierarchical leaf architecture of the Silversword, a dual scale core-shell fiber membrane was fabricated by combining coaxial electrospinning with in situ hydrothermal growth of ZnO nanorods. A PVDF-modified PEG/PAN core-shell architecture enabled the formation of a ZnO-nanorod scattering exterior while retaining the phase-transition behavior of the PEG-containing core after hydrothermal processing. This spatially separated architecture assigns distinct thermal-management roles to the two domains: the ZnO exterior reduces solar heat loading, whereas the PEG-containing core buffers transient temperature variation through reversible latent-heat storage and release.The resulting phase-change radiative fiber membrane (PRFM) exhibited a solar reflectivity of 91%, an atmospheric-window emissivity of 85%, and a melting enthalpy of 59.6 J/g. Under repeated simulated solar irradiation at approximately 1000 W/m², PRFM showed suppression of temperature rise. During the third irradiation cycle, its temperature was more than 6 °C lower than that of the control. In the outdoor device test, PRFM achieved a maximum temperature reduction of 5.3 °C relative to PAN during the high irradiance period. After 500 twisting-spreading cycles, the membrane retained 86.4% of its initial latent heat. When attached directly to the arm in the outdoor wearable test, it maintained an average temperature 4.6 °C lower

than that of commercial cotton. This work provides a structural strategy for integrating optical heat-load regulation and latent-heat buffering within a single fibrous platform.
KEYWORDS: phase-change nanofibers; ZnO nanoarrays; hydrothermal mineralization; radiative cooling; transient thermal buffering

Just Accepted

1 Introduction

Passive personal thermal management (PTM) materials aim to reduce the local thermal burden associated with solar exposure without relying on external energy input [1–3]. This objective is increasingly important for outdoor work, protective clothing, transportation, and other situations in which the microclimate near the human body is exposed to intense solar radiation. Conventional cooling technologies, including air conditioning and refrigeration, can provide effective temperature control but require continuous energy consumption and are not readily applicable to localized or wearable scenarios [4, 5]. In contrast, textile-based passive thermal-management materials regulate radiative, conductive, convective, and moisture-related heat transfer through their intrinsic composition and structure [6–8]. Among the available strategies, daytime passive radiative cooling (PRC) and phase-change energy storage are particularly relevant because they address different stages of heat accumulation and dissipation [9, 10].

Passive radiative cooling (PRC) materials operating in the daytime reduce solar heat gain by reflecting incident sunlight, typically across the 0.3–2.5 μm range, while simultaneously emitting thermal radiation through the atmospheric window at 8 and 13 μm [11–14]. For wearable applications, electrospun fiber membranes are attractive radiative-cooling substrates because their porous and multiscale structures can provide efficient light scattering, low areal density, mechanical flexibility, and vapor transport [15–18]. Inorganic particles or nanostructures, including ZnO, TiO_2 , and SiO_2 , are often incorporated to increase the refractive-index contrast and construct photon-scattering interfaces [19–22]. Nevertheless, radiative cooling primarily regulates the radiative heat balance. Under transient solar exposure, changing wind conditions, body movement, or intermittent shading, a material with high solar reflectivity may still experience relatively rapid temperature fluctuations because its thermal response depends on the instantaneous balance among absorbed radiation, convection, conduction, and infrared emission [23, 24].

Phase-change materials (PCMs) provide a complementary route for thermal regulation. Through reversible melting and crystallization, PCMs absorb heat during temperature rise and release stored heat during temperature decrease, thereby moderating the rate and amplitude of transient temperature variation [25–28]. Polyethylene glycol (PEG) is one of the most widely studied organic PCMs, owing to its suitable transition temperature, high latent enthalpy, commercial availability, and low toxicity [29, 30]. For textile applications, PEG is commonly encapsulated in polymer matrices, microcapsules, or core-shell fibers to reduce leakage and improve processability [31–33]. However, PCM-based fibers alone do not directly reduce the incident solar heat load. Under prolonged irradiation, once the phase transition is complete, the stored latent heat is exhausted and the temperature begins to rise again[34–36]. Therefore, combining radiative heat-load reduction with latent-heat buffering is a logical strategy for extending thermal regulation under solar exposure [37–39]. In such a system, the radiative-cooling component can reduce the rate of heat input, whereas the PCM can delay temperature increase near its transition range and moderate subsequent cooling through latent-heat release.

Despite this complementarity, integrating radiative cooling and phase-change storage into a single fibrous platform is not simply a matter of combining a reflective component with a PCM. Electrospun core-shell fibers provide a useful architecture for spatially separating functional components: the shell can provide mechanical support and an optical interface, while the core can accommodate a phase-change domain. However, a critical processing incompatibility emerges when an inorganic scattering layer is constructed through aqueous hydrothermal mineralization. Hydrothermal growth is an effective route for generating well-adhered ZnO nanoarrays on polymeric fiber surfaces, but it involves prolonged exposure to hot aqueous solution. Water-sensitive, low-molecular-weight PEG may diffuse, dissolve, or leach during this process, potentially reducing the latent-heat-storage function of the core [40–43]. This issue is particularly relevant for core-shell fibers because even when the PCM is initially confined within a polymer shell, water can penetrate through defects, pores, or interfacial pathways during hydrothermal treatment. Thus, the central materials challenge is to establish a fabrication route that enables the formation of a robust inorganic photon-scattering layer while preserving the functional phase-change domain.

The leaf of the Silversword (Argyroxiphium sandwicense) provides a useful structural analogy for addressing this challenge. Its hair-like outer surface motivates the design of a scattering-rich exterior that can interact with incident solar radiation, whereas its hydrated inner tissue suggests a thermally buffering interior. This study does not attempt to reproduce the biological thermoregulation mechanism of the plant. Instead,

Just Accepted

it translates the hierarchical architectural principle into a fiber membrane in which an external photon-scattering layer is combined with an internal PCM-containing domain. Such a design is meaningful only when the formation of the external mineralized layer does not substantially impair the phase-transition behavior of the core.

Herein, a phase-change radiative fiber membrane (PRFM) was prepared by coaxially electrospinning PVDF-modified PEG/PAN core-shell fibers, followed by seed-assisted hydrothermal growth of ZnO nanoarrays (Fig. 1). PAN provides the fibrous scaffold, while the $Zn(Ac)_2$ dispersed in the shell acts as the nucleation source for ZnO growth and PVDF is added to the PEG-containing core to suppress PEG leaching during aqueous processing. The structural evolution of the ZnO nanoarray, optical response, phase-transition behavior, and thermal-management performance of the hierarchical membrane were systematically investigated. Importantly, the material is evaluated not only by solar reflectivity, infrared emissivity, or latent heat as isolated parameters, but also by its ability to regulate solar-driven temperature trajectories under simulated irradiation, direct heating/cooling, outdoor device-level testing, and a wearable proof-of-concept comparison.

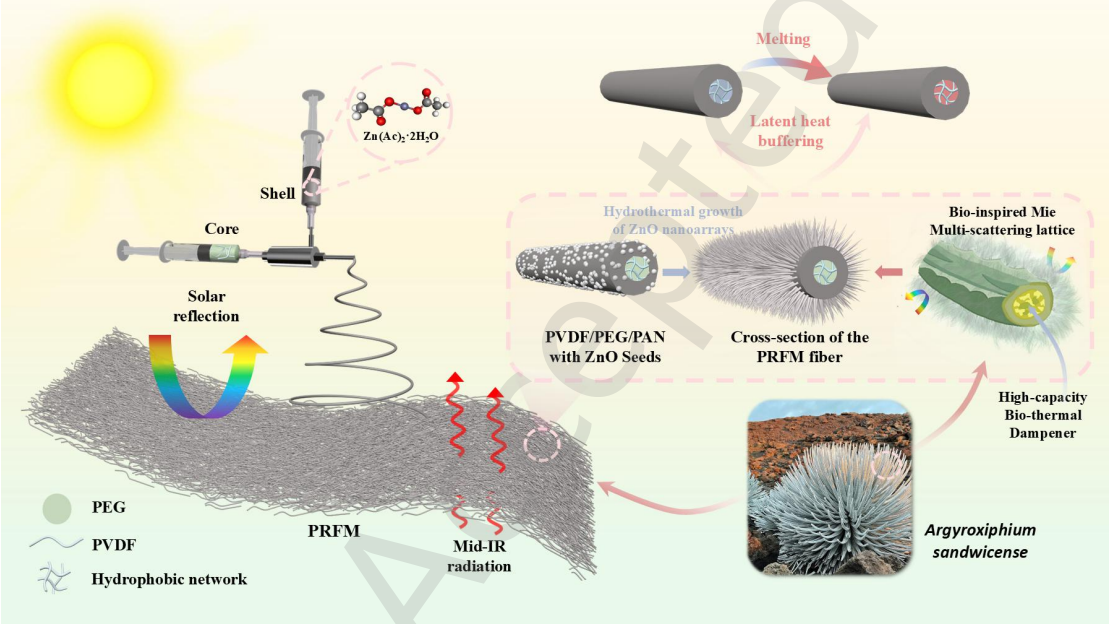


Figure 1 Structure design and fabrication process of PRFM

2 Results and Discussion

2.1 Structural evolution of PRFM

The construction of PRFM began with the preparation of a PEG/PAN core-shell fiber membrane. As shown in Fig. 2(a), PEG/PAN-0.7 (The number represents the weight fraction of PEG in the core solution) formed a flexible white membrane with a thickness of approximately 80 μm. The corresponding SEM image reveals a continuous fibrous network (Fig. 2(b)). Compared with pristine PAN fibers, whose diameters were mainly distributed between 0.18 and 0.32 μm (Fig. S1(a), (b)), PEG/PAN-0.7 exhibited an increased average fiber diameter of 0.44 ± 0.15 μm (Fig. S1(c)), consistent with the introduction of a PEG-containing core. This composition was selected as the precursor platform because it maintained a continuous fibrous morphology while providing phase-change capacity.

Because the subsequent growth of ZnO involves aqueous hydrothermal treatment, PVDF was incorporated into the PEG-containing core before mineralization. The effect of PVDF content was first evaluated after 10 h of ZnO growth. As shown in Fig. 2(c), the measured phase-change enthalpy increased over the investigated PVDF-content range. However, when the PVDF content reached 3 wt%, the core suspension became visibly inhomogeneous, with PVDF-rich aggregates appearing in the PEG phase. Therefore, 2 wt% PVDF was selected for subsequent fabrication as a balance between the measured phase-change response and the dispersion uniformity of the core spinning suspension.

The PVDF-modified core-shell fibers were then used as substrates for hydrothermal ZnO growth. The surface morphology evolved with reaction time, as illustrated in Fig. 2(d) and Fig. S2. At relatively short reaction times, ZnO nanorods were sparsely distributed on the fiber surface. With prolonged hydrothermal treatment, the nanorods

Just Accepted

became more developed, and the surface coverage increased. A dense rod-like surface layer was obtained after 10 h, whereas further extension of the reaction time led to less uniform coverage. This trend is consistent with changes in precursor availability and competitive axial and lateral growth. Accordingly, a hydrothermal duration of 10 h was selected for PRFM preparation.

The resulting surface morphology also provides the basis for the Silversword-inspired structural analogy. As shown in Fig. 2(e), the dense trichome layer on the leaf surface of Argyroxiphium sandwicense resembles the rod-decorated exterior of PRFM. In this design, the ZnO nanorods constitute a scattering-rich outer layer, while the PEG-containing core serves as an internal latent-heat-buffering domain. This analogy is used to explain the architectural rationale of combining an external optical-regulation layer with an internal thermal-buffering layer, rather than to imply that PRFM reproduces the biological thermoregulation mechanism of the plant.

The hierarchical fiber structure was further examined after mineralization. The cross-sectional SEM image in Fig. 2(f) shows that the fiber membrane retained its core-shell-derived architecture, which resembles the aqueous tissue of the silversword plant for thermal buffering. Meanwhile, the average fiber diameter increased to 0.82 ± 0.24 μm after ZnO growth (Fig. S1(d)), reflecting the formation of the external nanorod layer. PRFM also preserved an interconnected porous structure, with pore sizes ranging from 0.62 to 4.96 μm and an average pore size of 4.77 μm (Fig. S3).

The strong fluorine-ether intermolecular interactions and dipole-dipole alignments between PVDF and PEG chains establish an interconnected semi-interpenetrating polymer network. This structural confinement imposes a high thermodynamic barrier that effectively suppresses the mobility and subsequent macro-phase leaching of PEG molecules during high-temperature water-bath processing, thereby addressing the structural degradation common in conventional physical blends (Fig. 2(g)). Such a robust intermolecular physical crosslinking network, governed by strong fluorine-ether interactions, establishes the micro-electrostatic foundation for fabricating the hydrothermally resilient anti-dissolution shield. The TEM image (Fig. 2(h)) reveals that the PEG core is uniformly encapsulated by the PAN shell containing $Zn(Ac)_2$. TEM characterization of PRFM (Fig. 2(i)) elucidates the uniform distribution of ZnO nanorods on the fiber surface without disrupting the internal core-shell structure, thereby verifying the effectiveness of the physical crosslinking network. Compared with the sprayed ZnO-particle sample, the hydrothermal route produced a more continuous surface coverage in the observed images (Fig. S4).

Based on these structural observations, the proposed construction logic of PRFM is that the PAN provides the continuous fibrous scaffold and the interface for ZnO mineralization; the PVDF-modified PEG-containing core forms the internal phase-change domain; and the hydrothermally grown ZnO nanorods create the external scattering layer. Thus, the final membrane integrates a trichome-like ZnO exterior with a PCM-containing core in a single hierarchical fibrous architecture.

Just Accepted

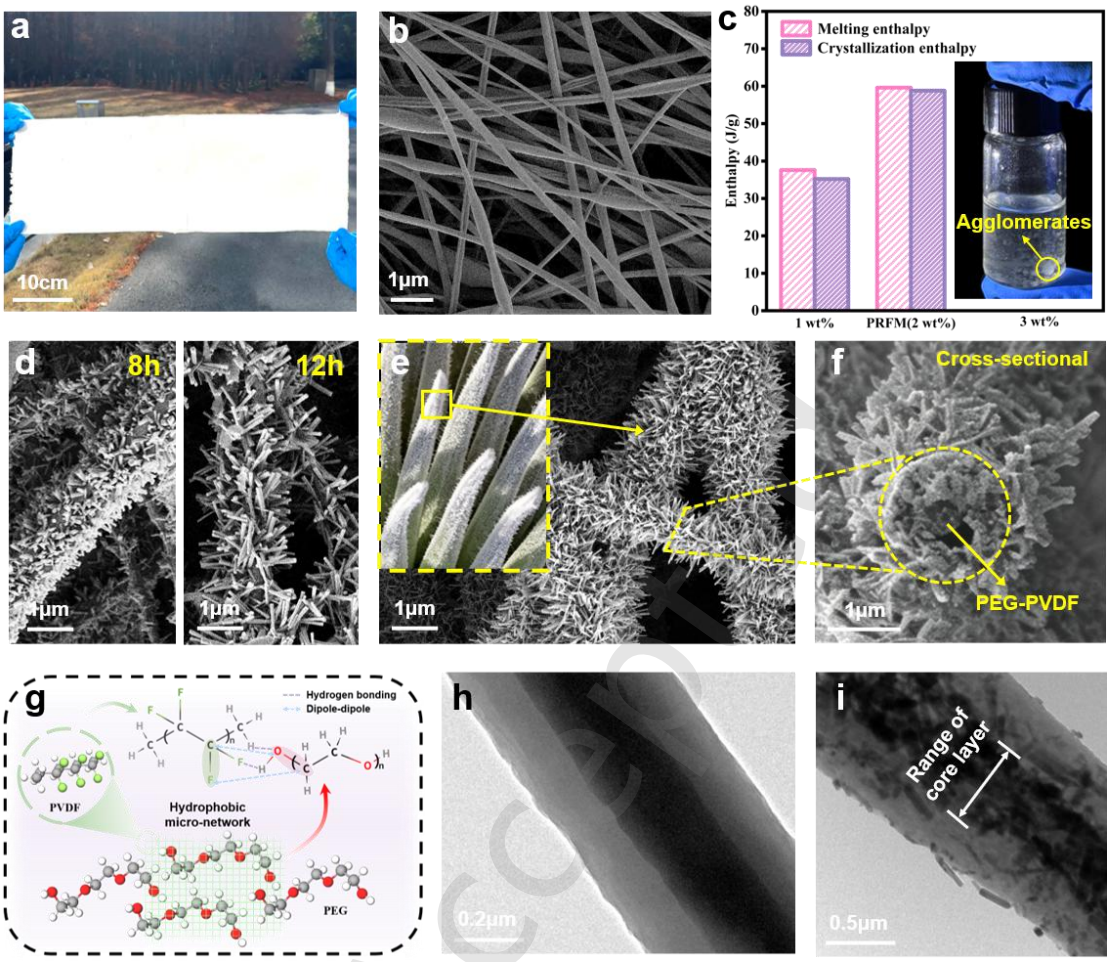


Figure 2 Structural evolution of PRFM. (a) Photograph of PEG/PAN fiber membrane. (b) SEM images of PEG/PAN-0.7 fiber membrane. (c) Enthalpies of fiber membranes with different PVDF contents after 10 h of hydrothermal ZnO growth, and the core solution photograph at 3 wt% PVDF. (d) SEM images of PVDF/PEG/PAN/ZnO-Y (Y = 8 and 12). (e) Photograph of Argyroxiphium sandwicense and SEM image of PRFM. (f) Cross-sectional SEM image of PRFM. (g) Schematic diagram of the mechanism for constructing a hydrophobic framework structure with PVDF. (h) TEM image of PEG/PAN-0.7 fiber membrane. (i) TEM image of PRFM.

2.2 Optical and phase-change properties

To clarify the optical design of PRFM, finite-difference time-domain (FDTD) simulations were first performed and interpreted in conjunction with Mie scattering theory. ZnO was selected as the external scattering component because of its relatively high refractive index ($n \approx 2$) and low absorption across the visible-to-mid-infrared spectral range [44]. As shown in Fig. 3(a), ZnO nanorods with lengths of 0.25–0.50 μm exhibit pronounced scattering within the 400–800 nm region. In addition, fibers with diameters ranging from 0.6 to 1.6 μm show high scattering efficiencies over a broader portion of the solar spectrum (Fig. 3(b)). These simulations indicate that the combined length scale of the ZnO nanorods and the PRFM fibers is favorable for enhancing solar scattering, which is highly consistent with Mie scattering theory [45]. The design is structurally inspired by the dense surface trichomes of the Silversword leaf, which provide a scattering-rich outer interface under strong solar irradiation.

The chemical composition of the membranes was examined by FTIR spectroscopy (Fig. 3(c)). PAN, PEG/PAN-0.7, and PRFM all show the characteristic stretching vibration of PAN at 2244 cm^{-1}, corresponding to the –C≡N group. The PEG-containing samples exhibit characteristic ether-related absorption bands associated with –C–O– and –C–O–C– vibrations. After hydrothermal treatment, PRFM retains the characteristic PEG-related bands, together with the C–F vibration of PVDF at 880 cm^{-1} and the β-phase-related absorption band near 840 cm^{-1}. A new absorption peak at 509 cm^{-1} is assigned to Zn–O stretching vibration, confirming the formation of ZnO nanostructures on the fiber surface [46, 47]. These results demonstrate the

coexistence of the PEG-containing phase-change domain, the PVDF-containing core component, and the ZnO outer layer in PRFM.

The optical response of PVDF/PEG/PAN/ZnO-Y (Y = 2, 4, 6, 8, 10) membranes prepared with different hydrothermal durations was further evaluated using a UV–Vis–NIR spectrophotometer equipped with an integrating sphere. As shown in Fig. 3(d), the solar reflectivity initially increased with hydrothermal growth time and reached 91% for PRFM prepared at 10 h, as calculated using Equation (1). A further extension of the reaction time led to lower average reflectivity (Fig. S5), consistent with the less uniform nanorod coverage observed at prolonged growth durations. The high reflectivity of PRFM can therefore be attributed to the dense ZnO nanorod layer together with the fibrous porous substrate, which introduces multiple scattering events for incident solar radiation.

Based on Kirchhoff's law of thermal radiation, for an optically opaque membrane, the emissivity can be estimated from the measured reflectivity. The mid-infrared optical response is presented in Fig. 3(e). PEG/PAN-0.7 exhibits an average emissivity of 83.32% within the atmospheric window, while PRFM reaches 85% after ZnO growth (calculated using Equation (2)). The slightly higher value for PRFM is associated with the combined infrared response of the PEG-containing phase-change component, PVDF, and ZnO nanorod surface layer. Thus, the hydrothermally generated outer structure contributes to solar scattering while maintaining a high mid-infrared radiative response.

The thermal stability of the membranes was assessed by thermogravimetric analysis under nitrogen (Fig. 3(f)). PEG/PAN-0.7 displays a major weight-loss stage in the range of 300–450 °C, which is associated with the decomposition of PEG, whereas PAN undergoes decomposition at higher temperatures. Despite the presence of PVDF in PRFM, the overall thermal decomposition behavior of PEG is comparable to that of PEG/PAN-0.7. PRFM exhibits a higher residual mass than PAN and PEG/PAN-0.7, mainly because of the inorganic ZnO content. Together with the FTIR results, the TGA profiles further support the successful incorporation of ZnO into the composite membrane.

The phase-transition behavior and latent-heat-storage capability were evaluated by DSC between 0 and 50 °C (Fig. 3(g), (h)). Pure PAN shows no apparent phase-transition peak in this temperature range, whereas pure PEG exhibits melting and crystallization peaks at approximately 41.0 and 26.7 °C, respectively. The PEG-containing core-shell membranes retain similar phase-transition behavior, indicating that the PCM remained functional after fiber formation. As the PEG concentration increased, the melting enthalpy increased from 42 to 82 J/g, while the crystallization enthalpy increased from 40.3 to 79 J/g. However, PEG/PAN-0.8 showed noticeable leakage during melting, indicating that further increasing PEG loading compromised structural stability (Fig. S6). Therefore, PEG/PAN-0.7 was selected as the precursor platform by balancing latent-heat capacity and membrane integrity.

Replicate experiments confirmed that the enthalpy retention ratio of PRFM was significantly higher than that of PRFM without PVDF (Fig. 3(i)). The sample without PVDF addition, which was directly subjected to hydrothermal growth of ZnO, suffered from partial dissolution or leaching of PEG owing to prolonged exposure to the hot aqueous solution, retaining only 22.6% of the melting enthalpy and 12.9% of the crystallization enthalpy relative to PEG/PAN 0.7. After PVDF incorporation and ZnO mineralization, PRFM retained a melting enthalpy of 59.6 J/g and a crystallization enthalpy of 58.8 J/g, corresponding to approximately 72.7% and 74.4% of the respective values of PEG/PAN-0.7. These results provide quantitative evidence that the PVDF network effectively suppresses PEG leaching during hydrothermal treatment, thereby enabling the membrane to preserve a meaningful latent-heat-storage capacity. Consequently, PRFM integrates two complementary thermal-management functions: the ZnO-decorated exterior reduces solar heat input through enhanced scattering and infrared radiation, whereas the PEG-containing core moderates temperature variation through reversible latent-heat absorption and release. Moreover, after 50 heating-cooling cycles, the phase-transition temperatures of PRFM remained essentially unchanged, while the melting enthalpy decreased from 59.6 to 50 J/g (a retention of approximately 84%) (Fig. S7). This moderate decrease is likely due to trace PEG migration, slight fatigue of the PVDF physical crosslinking network, and a minor reduction in PEG crystallinity. Nevertheless, the retained latent heat indicates that the phase-change function remained stable over the tested cycling period.

In Press Accepted

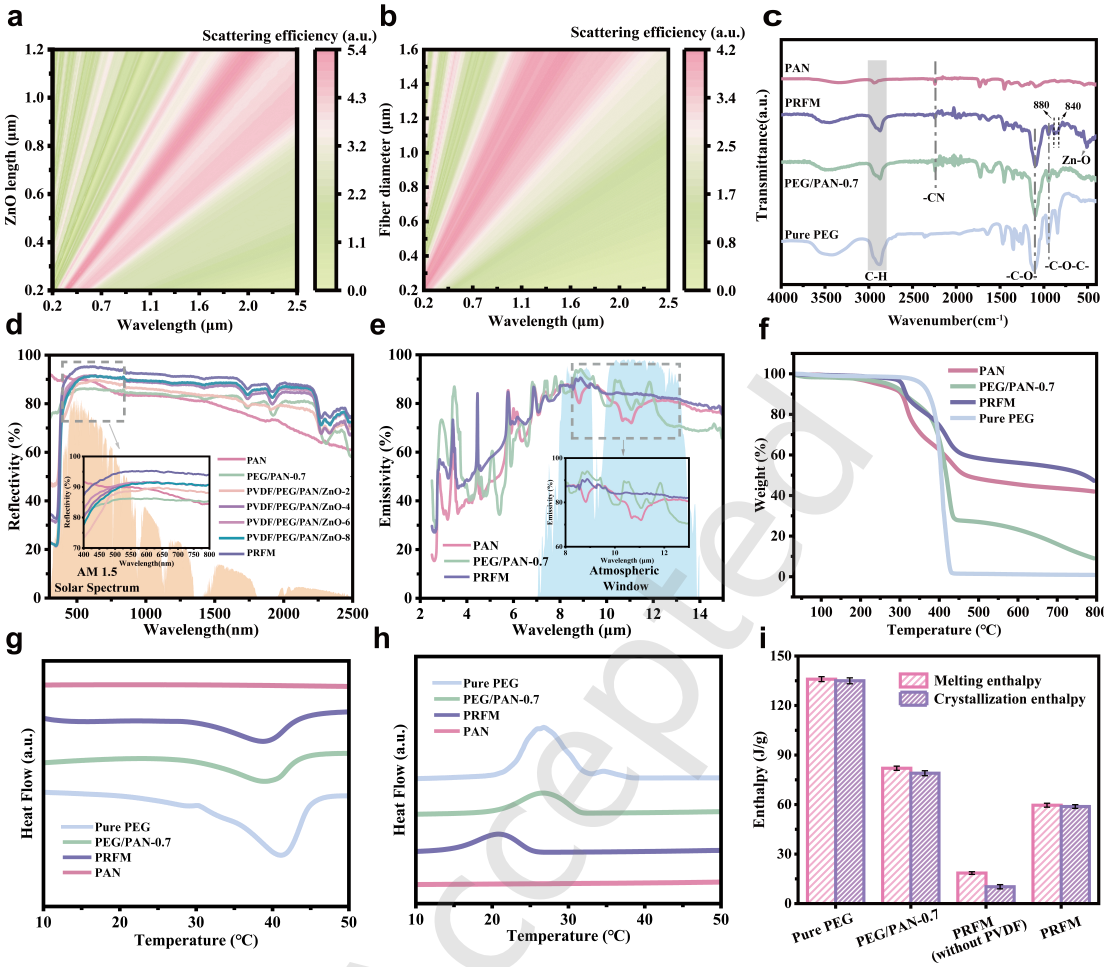


Figure 3 Optical and phase-change properties. Simulated scattering efficiency of (a) ZnO nanorods of different lengths and (b) PRFM fibers with different diameters in the solar spectrum. (c) FTIR spectra of fiber membranes and PEG. (d) Solar reflectivity and (e) mid-infrared emissivity of the fiber membranes. (f) TGA curves of the fiber membranes and pure PEG. DSC (g) heating and (h) cooling curves of the fiber membranes and pure PEG. (i) Melting and crystallization enthalpies of pure PEG, PEG/PAN-0.7, PRFM without PVDF, and PRFM.

2.3 Thermal management and temperature buffering behavior

The thermal-management behavior of PRFM was evaluated under simulated solar irradiation, contact heating, and outdoor exposure. As illustrated in Fig. 4(a), a xenon lamp was used to provide an irradiance of approximately 1000 W/m² at the sample position, while a constant-temperature heating platform was used to examine the transient thermal response under direct conductive heating. PAN/ZnO-10, which contains the ZnO surface layer but no PEG or PVDF in the core, was prepared as an optical-regulation control. PEG/PAN-0.7 was used to distinguish the contribution of the phase-change component from that of the ZnO-decorated outer layer.

Under repeated xenon-lamp on/off cycles, all samples showed distinct temperature trajectories (Fig. 4(b)). Compared with PAN, PAN/ZnO-10 exhibited a slower temperature rise under irradiation, indicating that the ZnO-decorated surface reduced the radiative heat load. PEG/PAN-0.7 also delayed the temperature increase, mainly because the PEG-containing core absorbed heat during melting. However, after the lamp was switched off, PAN/ZnO-10 cooled at a rate close to that of PAN, whereas PEG/PAN-0.7 exhibited a slower temperature decrease because of latent-heat release during PCM crystallization. PRFM combined these two effects. During the third heating cycle, the PAN control exceeded 50 °C, while PRFM remained below 44 °C, corresponding to a maximum temperature difference of 8.3 °C. After the final irradiation cycle, PRFM required 10.2 min to cool to 28 °C, which was 4.5 min longer than PAN. These results indicate that the ZnO nanorod layer primarily reduces solar heat input, whereas the PEG-containing core moderates both heating and cooling rates through reversible latent-heat storage.

The temperature-buffering effect was further

Just Accepted

examined on a heating platform maintained at 50 °C. Infrared thermograms in Fig. 4(c) show that PAN changed rapidly from blue to orange during heating, while PEG/PAN-0.7 and PRFM retained lower surface temperatures. The corresponding temperature profiles are presented in Fig. 4(d). After 100 s of heating, the temperatures of PAN, PEG/PAN-0.7, and PRFM reached 40.1, 38.8, and 37.4 °C, respectively. Thus, PRFM showed a maximum temperature reduction of 4.5 °C and an average temperature difference of approximately 3.0 °C relative to PAN during the heating period. After 120 s, PRFM still maintained a 2.1 °C temperature deficit relative to PAN.

The cooling behavior after removal from the heating platform should be interpreted as thermal buffering rather than additional cooling. PAN initially had the highest temperature but cooled most rapidly, becoming cooler than PRFM after approximately 60 s. Within 150 s, PAN cooled by 16.8 °C, which was 3.0 °C greater than the temperature decrease of PRFM. This slower cooling of PRFM is consistent with the release of stored latent heat during PEG crystallization. Therefore, PRFM does not simply lower temperature under every condition; instead, it suppresses the amplitude and rate of temperature variation around the PCM transition range.

The outdoor performance of PRFM was then assessed using the insulated test device shown in Fig. 4(e). The device consisted of a polystyrene foam enclosure to reduce conductive heat gain, an LDPE top film to limit convective exchange, and aluminum-foil-covered sidewalls to reduce lateral solar absorption. K-type thermocouples were used to monitor the temperatures beneath PAN, PEG/PAN-0.7, and PRFM, together with the temperature of the reference space inside the device. Accordingly, these results represent the thermal response of the membrane-device configuration rather than the free-exposure temperature of an unconstrained textile.

From 9:00 to 12:00, the average temperatures of the reference space, PAN, PEG/PAN-0.7, and PRFM were 40.2, 38.1, 35.3, and 31.6 °C, respectively (Fig. 4(f)). The relatively gradual temperature increase in the shaded interval is consistent with heat absorption by PEG during phase transition. From 13:00 to 15:00, the corresponding average temperatures were 34.5, 32.0, 30.1, and 27.8 °C. During the peak solar period, PRFM showed a maximum temperature reduction of 5.3 °C relative to PAN. The delayed temperature decrease observed in the afternoon is also consistent with latent-heat release from the PEG-containing core. These results suggest that the ZnO nanorod surface reduces solar heating, while the PCM core broadens the thermal-response timescale and attenuates temperature fluctuations.

Based on the steady-state energy balance, the limiting cooling power of PRFM was calculated. Fig. 4(g) illustrates the net cooling power as a function of the temperature difference under different non-radiative heat transfer coefficients (h_c). Under an assumed solar irradiance of 600 W/m², the maximum theoretical net cooling power was 66.9 W/m². Taken together, the simulated-solar, contact-heating, and outdoor tests demonstrate that PRFM regulates the temperature trajectory through the complementary actions of external solar scattering and internal latent-heat buffering.

Just Accepted

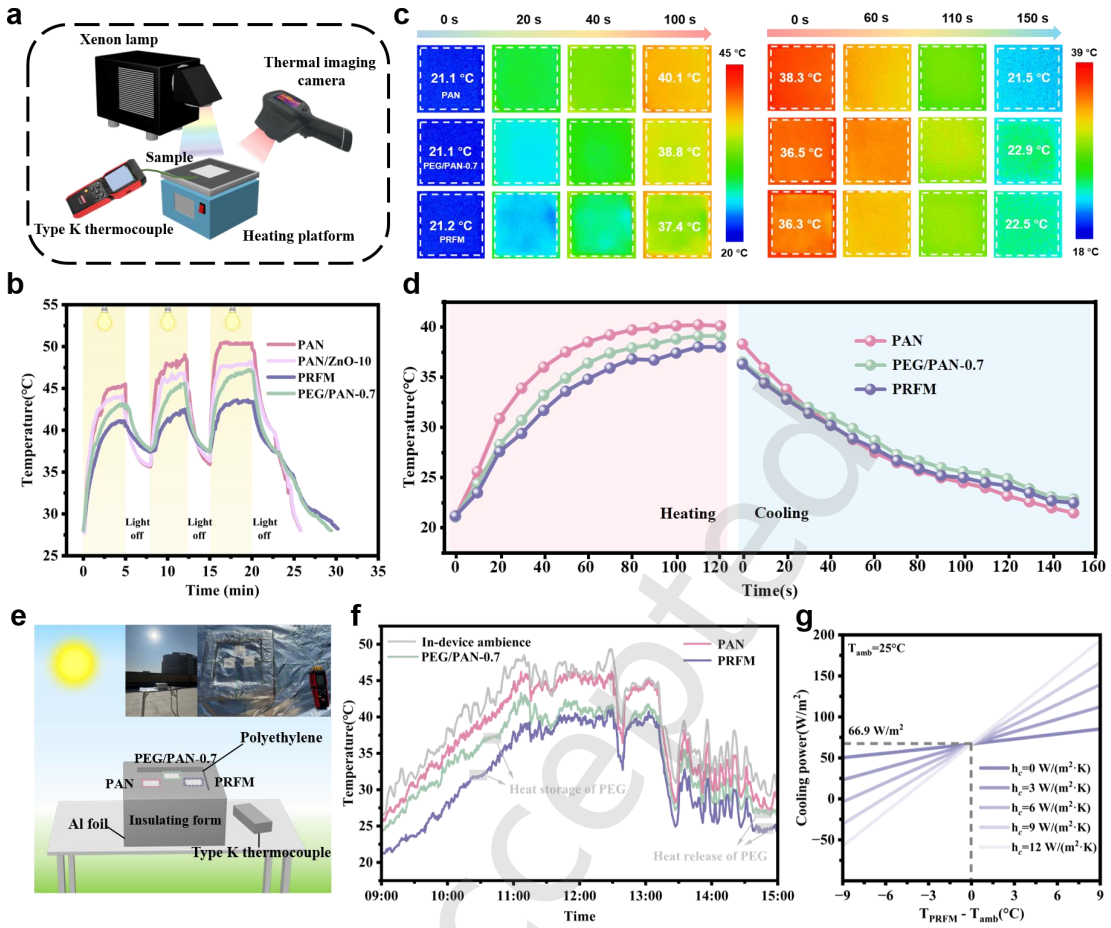


Figure 4 Thermal management and temperature buffering behavior. (a) Schematic diagrams of xenon lamp simulation of solar heating experiment and the temperature-controlled heating platform heating experiment. (b) Temperature rise and fall curves below the fiber membranes under xenon lamp under repeated xenon lamp on/off cycles. (c) Infrared thermograms of the fiber membranes during heating (right) and cooling (left). (d) Temperature rise and fall curves of the fiber membranes on the constant-temperature heating platform. (e) Photographs and schematic diagrams of the outdoor experimental setup. (f) Temperature curves for the in-device ambience, PAN, PEG/PAN-0.7, and PRFM in Hangzhou, China, on October 28, 2025, from 9:00 to 15:00. (g) Theoretical net cooling power of PRFM.

2.4 Wearability, durability, and outdoor demonstration

The mechanical properties, moisture-vapor transmission, and air permeability of the membranes were evaluated to assess their suitability for wearable thermal-management applications. Fig. 5(a) shows the stress-strain curves of the fibrous membrane under relatively low-temperature (20 °C) and simulated high-temperature (35 °C) test conditions. Pristine PAN exhibited relatively high tensile strength and elongation because of its continuous fibrous network. After introducing the PEG-containing core, PEG/PAN-0.7 showed lower tensile strength and fracture strain. This decrease may be associated with the restricted chain mobility of PEG below its phase change temperature (Fig. S8). Once PEG melts, the mechanical properties of both PEG/PAN-0.7 and PRFM are improved to some extent. After ZnO nanorods growth, PRFM displayed an average tensile strength of 4.2 MPa across both low and high temperature conditions. The recovery in tensile strength relative to PEG/PAN-0.7 is consistent with the contribution of the mineralized surface layer and the interfacial interaction between the ZnO nanorods and fibrous substrate. These results indicate that the hydrothermal mineralization process did not cause a further deterioration of the membrane's tensile performance. In assessing long-term wearability for high-temperature environments, PRFM retained 96.2% of its tensile strength and 97.6% of its elongation at break after 500 bending-recovery cycles, demonstrating excellent flexibility that meets the requirements for practical wearable applications (Fig. S9).

Moisture vapor transmission and air permeability were subsequently measured to evaluate the transport properties of PRFM. As shown in Fig. 5(b), PAN exhibited the highest

Just Accepted

water-vapor transmission value of 0.118 g/cm², which can be attributed to its interconnected porous structure. Incorporation of PEG reduced the value because the core component partially occupied the available pore space. After ZnO growth, PRFM retained a water-vapor transmission value of 0.1065 g/cm², which was slightly higher than that of the tested cotton fabric (0.1036 g/cm²). The limited decrease after mineralization suggests that the ZnO nanorods did not completely block the interconnected pores of the electrospun membrane.

Air permeability results are shown in Fig. 5(c). At a pressure differential of 100 Pa, PRFM showed an air permeability of 36.12 mm/s. Although this value was lower than that of commercial cotton fabric (63.9 mm/s), it remained substantially higher than that of commercial denim (approximately 8 mm/s) [48]. The reduced air permeability relative to cotton is reasonable because the ZnO-decorated fibers increase the flow resistance within the porous membrane. Nevertheless, the retained air permeability, together with the water-vapor-transmission result, indicates that the hierarchical structure can preserve a degree of vapor and air transport after functionalization.

The mechanical durability of the phase-change function was examined through 500 twisting-spreading cycles. As shown in Fig. 5(d), (e), PRFM retained 86.4% of its initial latent heat after cyclic deformation. Although a slight shift in phase-transition temperature was observed, the transition remained within the temperature range relevant to personal thermal management. This result shows that the membrane maintained most of its latent-heat-storage capability after the tested mechanical cycling.

Wearable thermal behavior was further demonstrated using commercial cotton and polyester fabrics as controls. Under indoor natural daylight (25 °C, 47 ± 3% relative humidity), the surface temperature of PRFM attached to medical protective clothing was on average 2.8 °C lower than that of commercial cotton within 10 min (Fig. 5(f)). When the materials were placed on the volunteer's arm, PRFM exhibited average surface temperatures 2.1 °C and 1.4 °C lower than polyester and cotton, respectively. These observations are consistent with the combined optical and latent-heat-buffering functions of PRFM, although the result should be regarded as a proof-of-concept comparison because it was obtained from a wearable demonstration.

Over the following days, outdoor tests were conducted under sunny conditions with ambient temperature of 30 ± 2 °C and humidity of 45–50% (Fig. 5(g)). When attached to a white cotton T-shirt, PRFM showed an average temperature 2.7 °C lower than commercial cotton during the 30 min test. When attached directly to the arm, the average temperature difference between PRFM and cotton reached 4.6 °C. Infrared thermography further showed that the PRFM surface temperature was up to 4.8 °C lower than bare skin and 3.5 °C lower than cotton. When both fabrics were attached to the arm, the maximum reductions relative to bare skin and cotton were 8.7 and 3.2 °C, respectively (Fig. S10). These results support the potential of PRFM for wearable thermal management under the tested conditions.

Just Accepted

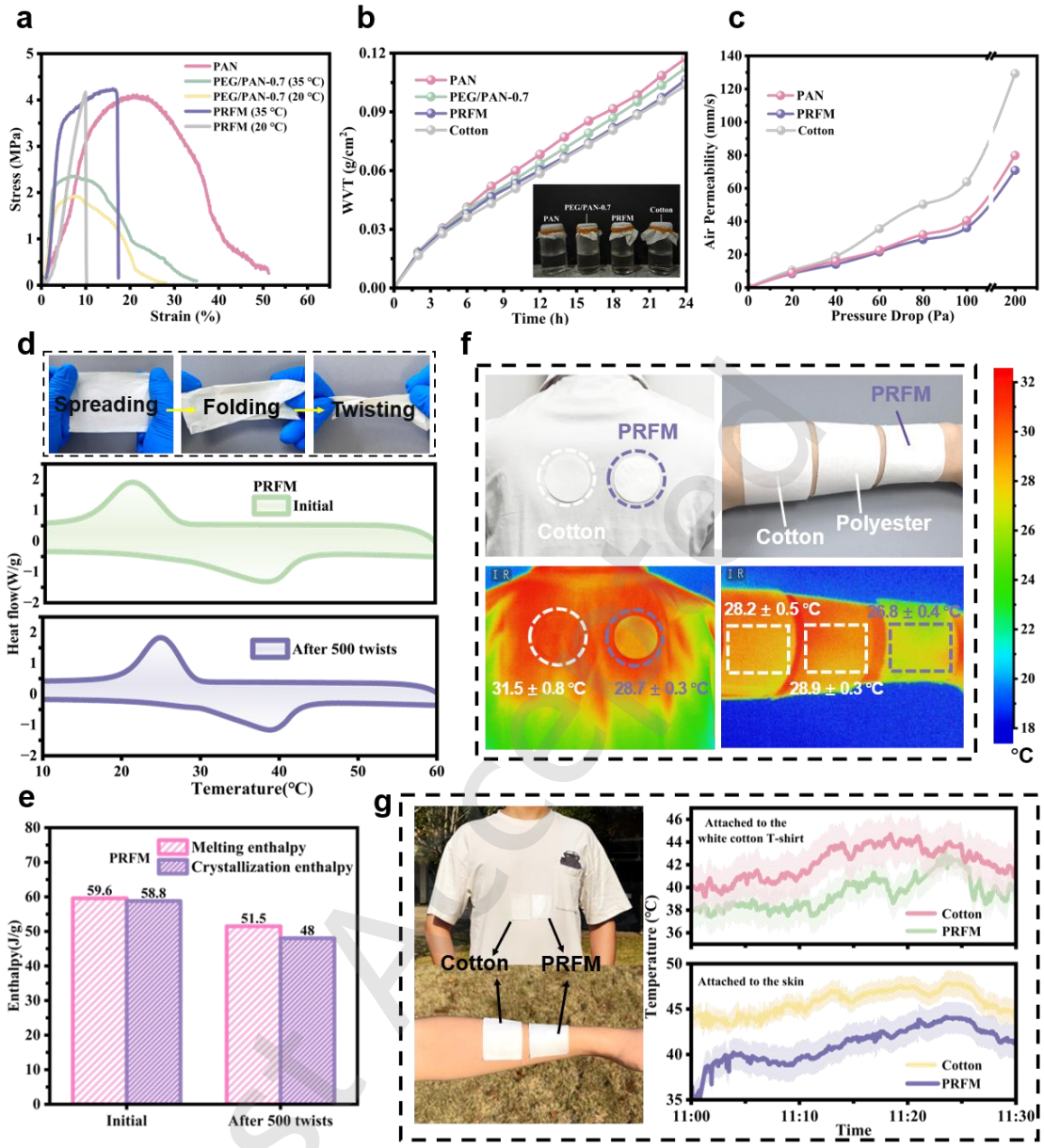


Figure 5 Wearability, durability, and outdoor demonstration. (a) Stress-strain curves of fiber membranes at different temperatures. (b) Moisture vapor transmission and (c) air permeability of fiber membranes. (d) DSC curves of the PRFM before and after 500 twisting cycles (applying one twist) and (e) corresponding melting and crystallization enthalpies. (f) Photographs and infrared thermograms of PRFM, cotton, and polyester attached to the back and arm skin of volunteer indoors. (g) Outdoor cooling performance and photographs of cotton and PRFM.

3 Conclusions

This work addresses the processing incompatibility between a water-sensitive phase-change core and hydrothermal mineralization required for constructing an inorganic photonic surface. Inspired by the hierarchical leaf architecture of the Silversword, a core-shell fiber membrane was designed in which a PEG-containing phase-change domain was integrated with a PAN fibrous scaffold and an in-situ-grown ZnO nanorod exterior. Incorporation of PVDF into the core formulation enabled the fabrication of the ZnO-decorated composite membrane while retaining the phase-transition behavior of the PEG-containing core after hydrothermal processing.

The resulting architecture separates two complementary thermal-management roles within a single fiber membrane. The ZnO nanorods exterior provides a scattering-rich interface that reduces solar heat loading, whereas the PEG-containing core absorbs and releases latent heat near its phase-transition range. Consequently, PRFM regulates the temperature trajectory rather than acting only as a low-temperature surface. Under repeated simulated solar irradiation, PRFM remained below 44 °C in the third heating cycle, while PAN exceeded 50 °C, producing a maximum

JSAC Accepted

temperature difference of 8.3 °C. Under direct heating, PRFM suppressed the heating-stage temperature by up to 4.5 °C relative to PAN and subsequently released stored heat during cooling. The outdoor device test further showed a maximum temperature reduction of 5.3 °C relative to PAN during the high-irradiance period.

Therefore, the principal contribution of this study is a structural route for integrating hydrothermally grown optical nanostructures with a phase-change core in one fibrous platform, enabling the coordinated regulation of solar heat input and transient temperature variation. The retained phase-change enthalpy, thermal-cycle stability, mechanical durability, and wearable demonstrations support the feasibility of this design for personal thermal-management applications.

4 Experimental

4.1 Materials

Polyacrylonitrile (average Mw of 150,000) and Zinc acetate dehydrate ($Zn(Ac)_2{\cdot}2H_2O$, AR) were supplied by Shanghai Aladdin Chemical Co., Ltd., China. Polyethylene glycol (PEG, Mw 1000) was purchased from Shanghai Yien Chemical Technology Co., Ltd., China. Polyvinylidene fluoride powder (average Mw of 534,000) was obtained from Shanghai Macklin Biochemical Technology Co., Ltd., China. Hexamethylenetetramine (HMTA, $C_6H_{12}N_4$, AR), N, N-dimethylformamide (DMF, AR), N, N-dimethylacetamide (DMAc, AR), and zinc nitrate hexahydrate ($Zn(NO_3)_2{\cdot}6H_2O$, AR) were obtained from Sinopharm Group Chemical Reagents Co., Ltd. These materials were all technical grade and used without further purification.

4.2 Preparation of the Optimization Platform (PEG/PAN Core-Shell Membranes)

The fundamental core-shell fibrous platform was systematically optimized to determine the maximum load capacity of the phase-change constituent. For the shell precursor, a preliminary PAN solution was prepared by dissolving 1.2 g of PAN powder in 8.8 g of DMF under continuous magnetic stirring in a 40 °C water bath for 3 h. Subsequently, $Zn(Ac)_2{\cdot}2H_2O$ was incorporated into the shell matrix at a fixed weight ratio of 10:1 relative to PAN, followed by another 2 h of agitation until a completely homogeneous precursor was achieved. Concurrently, the core solutions were prepared by dissolving pure PEG at varying mass fractions in DMF, followed by stirring at 40 °C for 30 min.

Both solutions were independently drawn into separate 10 mL syringes mounted on a micro-syringe pump and interconnected to a customized coaxial electrospinning nozzle via high-precision PTFE tubing. Electrospinning was executed under a steady high voltage of 12 kV, maintained at an ambient temperature of 25 °C and a relative humidity of approximately 35%. The feeding rates for the shell and core layers were strictly regulated at 1 mL/h and 0.25 mL/h, respectively, with a tip-to-collector distance of 15 cm. After 4 h of continuous deposition, a series of unrefined coaxial fiber membranes with different core phase-change fractions were collected and designated as PEG/PAN-X (where X = 0.6, 0.7, and 0.8, representing the weight fraction of PEG in the core solution). Based on the comprehensive balance of structural integrity and latent heat output, the 70 wt% PEG composition (PEG/PAN-0.7) was systematically selected as the optimal matrix platform for subsequent functionalization.

4.3 Synthesis of Hydrothermally-Resilient Composite Membranes (PRFM)

To safeguard the water-sensitive polyether core from severe leaching and structural dissolution during the subsequent protracted aqueous mineral growth, a fluorocarbon-based defensive micro-network was introduced into the optimized core architecture. Specifically, 2 wt% of PVDF powder was co-blended with the optimized 70 wt% PEG fraction, partially dissolved in DMAc, and subjected to an intensive ultrasonic bath for 1 h to guarantee the formation of a highly stable and well-dispersed core suspension (Fig. S11). Maintaining identical coaxial electrospinning parameters as detailed in Section 4.2, the modified core suspension and the $Zn(Ac)_2$ -fortified PAN shell precursor were co-spun to yield hydrothermally stable PVDF/PEG/PAN composite fiber membranes.

To initiate the growth of the surficial photonic scattering lattice, the as-spun composite membranes were subjected to an annealing heat treatment at 110 °C for 5 h to drive off residual carboxylate ions and anchor a dense, uniform ZnO seed layer on the fiber sheaths. Crucially, although bulk organic PEG exhibits a lower thermal onset decomposition threshold, the encapsulated PEG molecules within these specific composite architectures remain remarkably stabilized and immune to volatilization or degradation at 110 °C. Fig. S12 records the weight change of the PRFM membrane before and after annealing. The average weight loss was only 2.3%, most of which was attributed to the conversion of $Zn(Ac)_2{\cdot}2H_2O$ to

Just Accepted

ZnO, indicating that no significant amount of PEG was lost during the heat treatment step. This thermal fortitude is established by the micro-electrostatic shields governed by the fluorine-ether interactions and the tight spatial confinement imposed by the surrounding PAN polymer sheaths.

Following the seeding process, well-aligned ZnO nanorod arrays were vertically grown via a low-temperature hydrothermal reaction. The precursor solution was prepared by dissolving 25 mmol/L of $Zn(NO_3)_2 \cdot 6H_2O$ and 25 mmol/L of $C_6H_{12}N_4$ in deionized water. The seeded fiber membranes were completely immersed in the freshly prepared reactant and sealed inside a Teflon-lined stainless steel autoclave. The hydrothermal mineralization was sustained at 85 °C for predefined durations, yielding samples labeled as PVDF/PEG/PAN/ZnO-Y (where Y denotes the reaction time of 2, 4, 6, 8, 10, 12, or 14 h). The optimal phase change and radiative cooling fiber membrane (PRFM) was harvested at a peak duration of 10 h (PVDF/PEG/PAN/ZnO-10). Finally, all functionalized samples were thoroughly rinsed via alternating washing cycles with deionized water and ethanol, followed by drying in a vacuum oven at 60 °C for 2 h.

4.4 Material characterizations

The samples' surface morphology and structural analysis were performed using scanning electron microscopy (SEM, Carl Zeiss Corporation) and transmission electron microscopy (TEM, JEM-2100, Japan). Fourier-transform infrared (FTIR) Spectroscopy was performed using a Nicolet-57000 FTIR spectrometer (Thermo Scientific Corporation) to determine the chemical composition of the material. Thermal performance was evaluated using a handheld infrared thermal imager (EXPEC 1810, China). Temperature data were recorded using a Type K thermocouple (UT325F, China). The mechanical properties of the test specimens were evaluated using an electronic universal testing machine (34TM-5, Shanghai Instron Testing Equipment Trading Co., Ltd.). Water vapor transmission rate was measured by the weight method. Specifically, a small glass vial is filled with 10 milliliters of distilled water and sealed with a textile sample and a rubber band. The sealed vial is then placed in an environment maintained at 30 °C and 50% relative humidity. The flask is weighed every 2 hours, with the mass loss representing water evaporation. The mass reduction is then divided by the bottle's mouth area to obtain the water vapor transmission rate. Air permeability was determined using the YG461E air permeability tester (Wenzhou Fangyuan Instrument Co., Ltd., China) in accordance with the differential pressure method specified in the GB/T 5453-1997 standard.

4.5 Optical characterization and Calculation

The optical properties of the samples were evaluated by measuring their reflectivity with a UH4150 UV–Vis–NIR spectrophotometer equipped with an integrating sphere. Additionally, the fiber membrane's infrared reflectivity was determined in the 2.5–15 μm range using a Thermo Fisher Scientific Nicolet iS50 FTIR spectrometer equipped with a gold-coated diffuse integrating sphere.

The equation for calculating the average solar radiation reflectivity in the UV-VIS-NIR band was as follows [49]:

$$\overline{S} = \frac{\int_{0.3}^{2.5} I_{\mathrm{solar}}(\lambda) \cdot R(\lambda) d\lambda}{\int_{0.3}^{2.5} I_{\mathrm{solar}}(\lambda) d\lambda} \quad (1)$$

Here, $R(\lambda)$ is the spectral reflectivity, and $I_{\mathrm{solar}}(\lambda)$ represents the function of solar spectral irradiance varying with wavelength. The relevant data originates from the ASTM G173 global solar spectrum, with the solar radiation spectrum ranging from 0.3–2.5 μm.

The equation for calculating the average atmospheric window emissivity was as follows [50]:

$$\overline{\varepsilon} = \frac{\int_{8}^{13} I_{\mathrm{BB}}(\lambda) \cdot \varepsilon(\lambda) d\lambda}{\int_{8}^{13} I_{\mathrm{BB}}(\lambda) d\lambda} \quad (2)$$

Where $\varepsilon(\lambda)$ is the spectral emissivity, and $I_{\mathrm{BB}}(\lambda)$ denotes the spectral radiance of an ideal blackbody as a function of wavelength at different temperatures. The atmospheric window spans wavelengths from 8 to 13 μm. The spectral emissivity of a blackbody at temperature T can be calculated using the following equation [50]:

$$I_{BB}(T,\lambda) = \frac{2hc^2}{\lambda^5} \frac{1}{e^{hc/(\lambda k_B T)} - 1} \quad (3)$$

where h is Planck's constant, κ_B is Boltzmann's constant, c is the speed of light in vacuum, and λ is the wavelength.

4.6 FDTD numerical simulation

The scattering efficiency and electric field distribution of the optical fiber were calculated using the Finite Difference Time Domain solution (FDTD, Lumerical). Perfectly Matched Layer (PML) boundary conditions were applied along the x, y, and z-axes. A full-field scattering source was employed to provide light in the 0.2–2.5 μm wavelength range. Scattering efficiency and electric field distribution were measured using a

Just Accepted

cross-section analysis group and a 2D monitor, respectively.

Electronic Supplementary Material: Supplementary material (Figures S1–S11) is available in the online version of this article at https://doi.org/10.26599/NR.2026.94909317.

Data availability

The data that support the findings of this study are available from the corresponding author upon reasonable request.

Acknowledgements

This research was supported by the Zhejiang Provincial Natural Science Foundation of China (No. LQN26E030020, No. LQN25E030001) and the Fundamental Research Funds of Zhejiang Sci-Tech University (No. 26202154-Y).

Declaration of competing interest

All the contributing authors report no conflict of interest in this work.

Author contribution statement

Chang Zhang: Conceptualization, Formal analysis, Data curation, Methodology, Writing - original draft. Furong Liu: Investigation, Methodology. Shengjie Dai: Validation, Visualization. Chen Zhang: Investigation, Resources. Fei Sun: Funding acquisition, Resources. Feichao Zhu: Resources. Bin Yu: Resources, Supervision. Yunfei Rao: Methodology, Funding acquisition, Resources, Project administration, Writing - review & editing.

Use of AI statement

None.

References

[1] Yu, H.; Lu, J.; Yan, J.; Bai, T.; Niu, Z.; Ye, B.; Cheng, W.; Wang, D.; Huan, S.; Han, G. Selective Emission Fabric for Indoor and Outdoor Passive Radiative Cooling in Personal Thermal Management. *Nano-Micro Lett.* **2025**, 17, 192.

[2] Jiang, W.; Liu, J.-Z.; Wang, Z.; Li, T.; Wang, Y.; Cai, H.; Xie, Z.; Zhuo, M.-P.; Wang, H.; Wang, X.-Q.; et al. Wearable Passive Thermal Management Functional Textiles: Recent Advances in Personal Comfort and Energy Harvesting Applications. *Adv. Fiber Mater.* **2025**, 7, 1677–1717.

[3] Tian, M.; Jiang, Q. Personal Thermal Management Strategies to Reduce Energy Consumption: Principles and Applications of New Materials with Bionic Structures. *Energy Build.* **2024**, 324, 114887.

[4] DeAngelo, J.; Azevedo, I.; Bistline, J.; Clarke, L.; Luderer, G.; Byers, E.; Davis, S. J. Energy Systems in Scenarios at Net-Zero CO2 Emissions. *Nat. Commun.* **2021**, 12, 6096.

[5] Vats, G.; Mathur, R. A Net-Zero Emissions Energy System in India by 2050: An Exploration. *J. Clean. Prod.* **2022**, 352, 131417.

[6] Guan, M.; Wang, G.; Li, J.; Rossi, R. M.; Zhu, M. Human Body-Interfacing Material Strategies for Personal Thermal and Moisture Management of Wearable Systems. *Prog. Mater. Sci.* **2023**, 139, 101172.

[7] Xu, R.; Zhu, Z.; Zhang, H.; Fan, W.; Guan, T.; Wei, Y.; Xu, W.; Hu, B.; Wan, J. Synergistic Material–Structure Engineering for Mid‐Infrared Thermal Management in Textiles. *Small* **2025**, 21, e09257.

[8] Dong, Y.; Tian, B.; Wang, C.; Zhang, G.; Hua, F.; Meng, W.; Li, C.; Yan, Y.; Cheng, Z.; Wang, F. Dynamic Radiative Cooling: Mechanisms, Strategies, and Applications for Smart Thermal Management. *Nano-Micro Lett.* **2026**, 18, 146.

[9] Hu, X.; Quan, B.; Shi, Z.; Zhao, X.; Lu, G.; Ding, Y.; Lai, J.; Qu, J.; Peng, Y.; Lu, X. Bioinspired Hierarchical Radiative‐Phase Change Hybrid Cooling Composite with Record‐Breaking Cooling Power. *Adv. Mater.* **2026**, 38, e10988.

[10] Wang, S.; He, Y.; Feng, R.; Wu, X.-W.; Su, J. Composite Phase Change Materials Coupled with Radiative Cooling for Asphalt Pavement Thermal Management. *Constr. Build. Mater.* **2024**, 457, 139476.

[11] Zhang, Y.; Chen, X.; Cai, B.; Luan, H.; Zhang, Q.; Gu, M. Photonics Empowered Passive Radiative Cooling. *Adv. Photonics Res.* **2021**, 2, 2000106.

[12] Yin, X.; Yang, R.; Tan, G.; Fan, S. Terrestrial Radiative Cooling: Using the Cold Universe as a Renewable and Sustainable Energy Source. *Science* **2020**, 370, 786–791.

[13] Liu, J.; Yan, X.; Wu, W.; Ji, B.; Zhong, Y.; Zhang, L.; Wang, B.; Feng, X.; Xu, H.; Mao, Z. Self‐Switching Dynamic Infrared Radiative Cooler Enabling Triple‐Mode Temperature Regulation. *Adv. Mater.* **2026**, 38, e11445.

[14] Xie, A.-Q.; Qiu, H.; Jiang, W.; Wang, Y.; Niu, S.; Zhang, K.-Q.; Ho, G. W.; Wang, X.-Q. Recent Advances in Spectrally Selective Daytime Radiative Cooling Materials. *Nano-Micro Lett.* **2025**, 17, 264.

[15] Gong, X.; Ding, M.; Gao, P.; Ji, Y.; Wang, X.; Liu, X.-Y.; Yu, J.; Zhang, S.; Ding, B. High-Performance Waterproof, Breathable, and Radiative Cooling Membranes Based on Nanoarchitectured Fiber/Meshworks. *Nano Lett.* **2023**, 23, 11337–11344.

[16] Xin, Y.; Wang, Q.; Fu, C.; Du, S.; Hou, L.; Wei, X.; Wang, H.; Wang, X. Alumina Fiber Membrane Prepared by Electrospinning Technology for Passive Daytime Radiative Cooling. *Adv. Funct. Mater.* **2025**, 35, 2413813.

[17] Son, S.; Lee, T. Y.; Chae, D.; Lim, H.; Ha, J.; Kim, Y. K.; Lee, H. Efficient Daytime Radiative Cooling Cover Sheet with Dual‐Modal Optical Properties. *Adv. Opt. Mater.* **2022**, 10, 2201771.

[18] Gao, Z.; Wang, Y.; Pan, Y.; Ma, J.; Liu, X.; Liu, C.; Shen, C. Moisture-Wicking Fabric for Radiation Cooling. *Nano Res.* **2025**, 18, 94907537.

[19] Ma, R.; Xue, T.; Han, T.; Wang, C.; Yin, Y. Dual Mode Switchable Janus Nano-ZnO/rGO Cellulose Fabric with Radiative Regulation and Sweat Transport for Personal Thermal Management. *Chem. Eng. J.* **2025**, 520, 165707.

Just Accepted

[20] Zhao, K.; Zhang, H.; Zhai, Q.; Guan, X.; Zhen, Q.; Cui, J. Scalable, Waterproof, Breathable, and Flexible Polyolefin-Elastomer/Polyethylene Glycol@Zinc Oxide Microfibrous Fabrics for Daytime Radiative Cooling Clothing. *ACS Appl. Mater. Interfaces* **2024**, 16, 46798–46809.

[21] Liu, W.; Guo, W.; Wang, Y.; Song, L.; Du, P.; Li, N.; Xiong, J. Improving Passive Daytime Radiative Cooling via Incorporation of Composite Nanoparticles into Sheath of PU-PVDF Core-Sheath Nanofiber Film. *Appl. Therm. Eng.* **2024**, 255, 123955.

[22] Wang, H.; Zhou, Y.; Guo, R.; Li, N.; Xiong, J. Bioinspired Mushroom-Clusters Composite Fibers for Large-Scale Continuous Production and Efficient Radiative Cooling. *Chem. Eng. J.* **2026**, 538, 176502.

[23] Dong, Y.; Zhang, X.; Chen, L.; Meng, W.; Wang, C.; Cheng, Z.; Liang, H.; Wang, F. Progress in Passive Daytime Radiative Cooling: A Review from Optical Mechanism, Performance Test, and Application. *Renew. Sustain. Energy Rev.* **2023**, 188, 113801.

[24] Fan, S.; Li, W. Photonics and Thermodynamics Concepts in Radiative Cooling. *Nat. Photonics* **2022**, 16, 182–190.

[25] Das, A.; Apu, M. M. H.; Akter, A.; Reza, M. M. A.; Mia, R. An Overview of Phase Change Materials, Their Production, and Applications in Textiles. *Results Eng.* **2025**, 25, 103603.

[26] Nie, B.; Palacios, A.; Zou, B.; Liu, J.; Zhang, T.; Li, Y. Review on Phase Change Materials for Cold Thermal Energy Storage Applications. *Renew. Sustain. Energy Rev.* **2020**, 134, 110340.

[27] Wu, X.; Bashir, A.; Tang, C.-Y.; Tsui, G. C.-P.; Li, Z.; Chen, N.; Zhang, Y.; Chen, Y.; Cui, J.; Zhuang, J.; et al. A Core-Shell Fiber Membrane with Synergistic Radiative Cooling and Thermal Buffering for All-Weather Personal Comfort. *Chem. Eng. J.*, **2026**, 535, 175318.

[28] Bai, L.; Zhang, S.; Ma, Z.; Dou, L.; Li, J. Bio-Inspired Multifunctional Composite Phase Change Films for Synergistic Thermal Management and Microwave Absorption. *Nano Res.* **2026**, 19, 94908229.

[29] Xu, X.; Sun, Y.; Wang, W.; Ju, L.; Shu, R.; Gu, H. An Overview of Polyethylene Glycol Composite Phase Change Materials: Preparation, Physicochemical Properties and Application. *J. Energy Storage* **2024**, 104, 114581.

[30] Yang, J.; Zhou, Y.; Yang, L.; Feng, C.; Bai, L.; Yang, M.; Yang, W. Exploring Next‐Generation Functional Organic Phase Change Composites. *Adv. Funct. Mater.*, **2022**, 32, 2200792.

[31] Zhu, Z.; Bashir, A.; Wu, X.; Liu, C.; Zhang, Y.; Chen, N.; Li, Z.; Chen, Y.; Ouyang, X.; Chen, D. Highly Integrated Phase Change and Radiative Cooling Fiber Membrane for Adaptive Personal Thermal Regulation. *Adv. Funct. Mater.* **2025**, 35, 2416111.

[32] Yan, Z.; Zhai, H.; Fan, D.; Li, Q. A Trimode Textile Designed with Hierarchical Core-Shell Nanofiber Structure for All-Weather Radiative Personal Thermal Management. *Nano Today* **2023**, 51, 101897.

[33] Das, M.; Ura, D. P.; Szewczyk, P. K.; Berniak, K.; Knapczyk-Korczak, J.; Marzec, M. M.; Pichór, W.; Stachewicz, U. Thermal Energy Storage Performance of Liquid Polyethylene Glycol in Core–Shell Polycarbonate and Reduced Graphene Oxide Fibers. *Adv. Compos. Hybrid Mater.* **2024**, 7, 123.

[34] Li, H.; Yu, A.; Li, M.; Cai, Z.; Chen, L.; Sun, J. Nano-Hybridized Phase Change Material Melt-Spun Fibers and Fabrics with Radiative Cooling/Solar Heating for Efficient All-Weather Personal Smart Thermal Regulation. *J. Energy Storage* **2026**, 168, 122667.

[35] Al-Masri, A.; Khanafer, K.; Sedaghat, A. Passive Thermal Management of PV Solar Panels Using Carbon Fiber-Enhanced Phase Change Materials: A Numerical and Optimization Study. *Int. Commun. Heat Mass Transf.* **2025**, 167, 109278.

[36] Liao, W.; Wang, R.; Wang, X.; Chen, L.; Zhao, X.; Xing, J.; Wang, J.; Xie, H. Thermal Energy Management and Utilization of High-Heat-Capacity Nickel Foam/Kapok Core-Shell Aerogel Composite Phase Change Materials. *Appl. Therm. Eng.* **2026**, 298, 131156.

[37] Ge, X.; Tay, G.; Hou, Y.; Zhao, Y.; Sugumaran, P. J.; Thai, B. Q.; Ang, C. K.; Zhai, W.; Yang, Y. Flexible and Leakage-Proof Phase Change Composite for Microwave Attenuation and Thermal Management. *Carbon* **2023**, 210, 118084.

[38] Qin, M.; Xiong, F.; Aftab, W.; Shi, J.; Han, H.; Zou, R. Phase-Change Materials Reinforced Intelligent Paint for Efficient Daytime Radiative Cooling. *iScience* **2022**, 25, 104584.

[39] Shamseddine, I.; Pennec, F.; Biwole, P.; Fardoun, F. Supercooling of Phase Change Materials: A Review. *Renew. Sustain. Energy Rev.* **2022**, 158, 112172.

[40] Soo, X. Y. D.; Tan, S. Y.; Cheong, A. K. H.; Xu, J.; Liu, Z.; Loh, X. J.; Zhu, Q. Electrospun PEO/PEG Fibers as Potential Flexible Phase Change Materials for Thermal Energy Regulation. *Exploration* **2024**, 4, 20230016.

[41] Guo, Y.; Hou, T.; Wang, J.; Yan, Y.; Li, W.; Ren, Y.; Yan, S. Phase Change Materials Meet Microfluidic Encapsulation. *Adv. Sci.* **2024**, 11, 2304580.

[42] Liu, Y.; Chen, X.; Gao, Y.; Yu, D.-G.; Liu, P. Elaborate Design of Shell Component for Manipulating the Sustained Release Behavior from Core–Shell Nanofibres. *J. Nanobiotechnology* **2022**, 20, 244.

[43] Wang, T.; Wei, R.; Wang, X.; Yang, Y.; Wang, Z.; Wang, Z.; He, Z.; Yi, S. Shape-Stabilized and Flexible Phase Change Materials with Enhanced Photothermal Conversion for Efficient Thermal Energy Storage. *Compos. Part B Eng.* **2025**, 302, 112539.

[44] Cai, L.; Song, A. Y.; Li, W.; Hsu, P.; Lin, D.; Catrysse, P. B.; Liu, Y.; Peng, Y.; Chen, J.; Wang, H.; et al. Spectrally Selective Nanocomposite Textile for Outdoor Personal Cooling. *Adv. Mater.* **2018**, 30, 1802152.

[45] Eslamisaray, M. A.; Wray, P. R.; Lee, Y.; Nelson, G. M.; Ilic, O.; Atwater, H. A.; Kortshagen, U. R. A Single-Step Bottom-up Approach for Synthesis of Highly Uniform Mie-Resonant Crystalline Semiconductor Particles at Visible Wavelengths. *Nano Lett.* **2023**, 23, 1930–1937.

[46] Rathod, P. P.; Bhosle, V. K.; Ubale, A. U.; Khan, Z. S. Ultrasonically Synthesized ZnO-GO Nanocomposite for Photocatalytic and Antibacterial Applications. *Compos. Commun.* **2025**, 57, 102457.

[47] Chandramohan, S.; Ramalingam, P.; Krishna, G. S.; Manikandan, E.; Rajagopalan, R. Multifaceted Investigation of Zinc Oxide Nanoparticles Synthesized from Vernonia Elaeagnifolia Leaf Extract: Characterization, Antibacterial, Antioxidant, Cytotoxicity, and DNA Binding Activities. *Inorg. Chem. Commun.* **2025**, 177, 114384.

[48] Zhang, X.; Yang, W.; Shao, Z.; Li, Y.; Su, Y.; Zhang, Q.; Hou, C.; Wang, H. A Moisture-Wicking Passive

Just Accepted

Radiative Cooling Hierarchical Metafabric. *ACS Nano* **2022**, 16, 2188–2197.

[49] Huang, X.; Li, N.; Wang, J.; Liu, D.; Xu, J.; Zhang, Z.; Zhong, M. Single Nanoporous $MgHPO_4 \cdot 1.2H_2O$ for Daytime Radiative Cooling. *ACS Appl. Mater. Interfaces* **2020**, 12, 2252–2258.

[50] Cho, J.-W.; Lee, Y.-J.; Kim, J.-H.; Hu, R.; Lee, E.; Kim, S.-K. Directional Radiative Cooling via Exceptional Epsilon-Based Microcavities. *ACS Nano* **2023**, 17, 10442–10451.

Just Accepted

Electronic Supplementary Material

Hydrothermally grown ZnO nanoarrays on phase-change core-shell fibers for solar heat-load reduction and thermal buffering

Chang Zhang [1,2], Yunfei Rao [1,2] ✉, Furong Liu [1,2], Shengjie Dai [1,2], Chen Zhang [3], Fei Sun [1,2] ✉, Feichao Zhu [1,2], Bin Yu [1,2] ✉

[1] State Key Laboratory of Bio-Based Fiber Materials, Zhejiang Sci-Tech University, Hangzhou 310018, China

[2] College of Textile Science and Engineering, Zhejiang Sci-Tech University, Hangzhou 310018, China

[3] Shanghai Science and Technology Exchange Center (SSTEC), Shanghai 200030, China

Supporting information to https://doi.org/10.26599/NR.2026.94909317

Just Accepted

Address correspondence to Yunfei Rao, yunfei.rao@zstu.edu.cn; Fei Sun, sunfei_92@zstu.edu.cn; Bin Yu, yubin7712@163.com

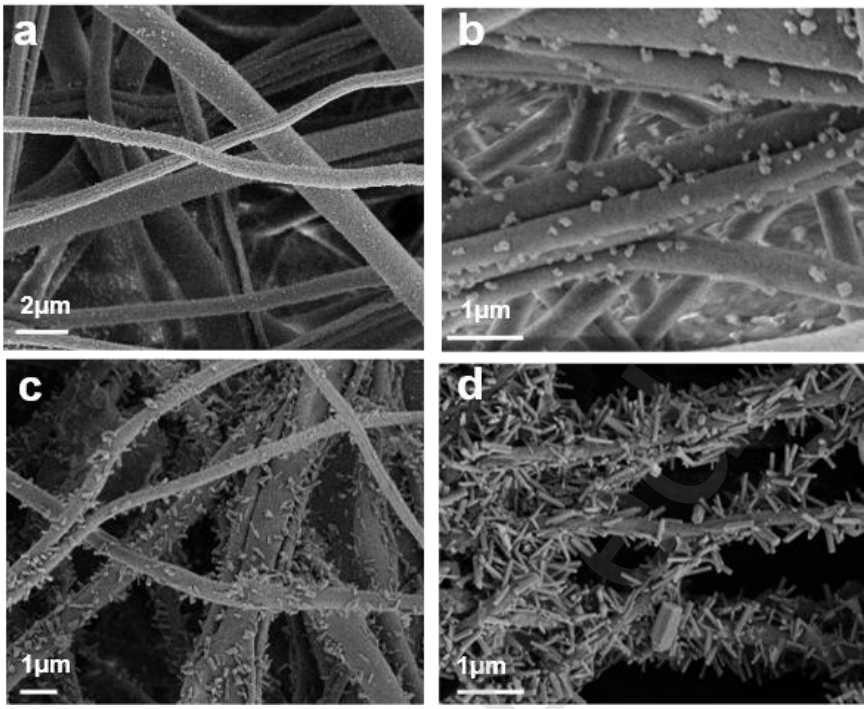


Figure S2 SEM images of PVDF/PEG/PAN/ZnO-Y (Y = 2 (a), 4 (b), 6 (c), 14 (d)) fiber membranes.

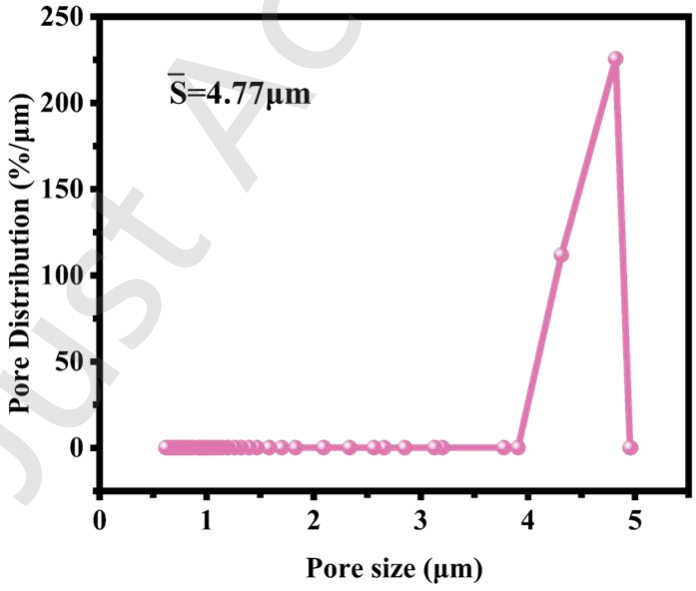


Figure S3 Pore size distribution of PRFM.

Just Accepted

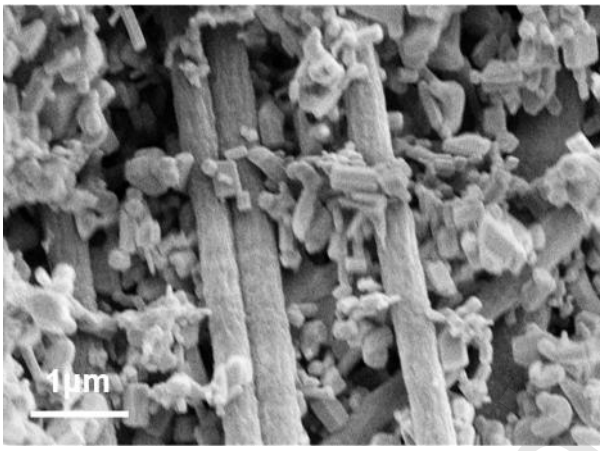


Figure S4 SEM image of the fiber membrane surface-sprayed with nano ZnO.

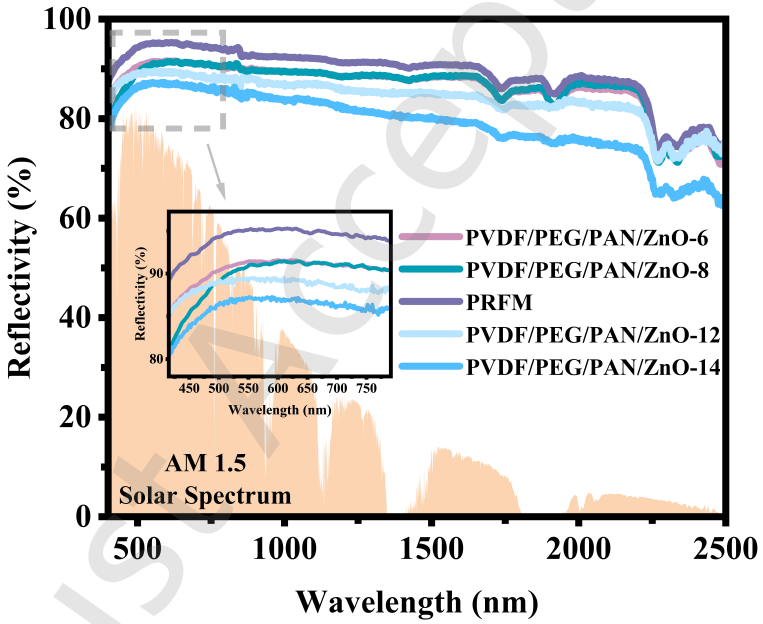


Figure S5 Solar radiation spectra of the PVDF/PEG/PAN/ZnO-Y (Y = 6, 8, 10, 12, 14) fiber membranes.

Just Accepted

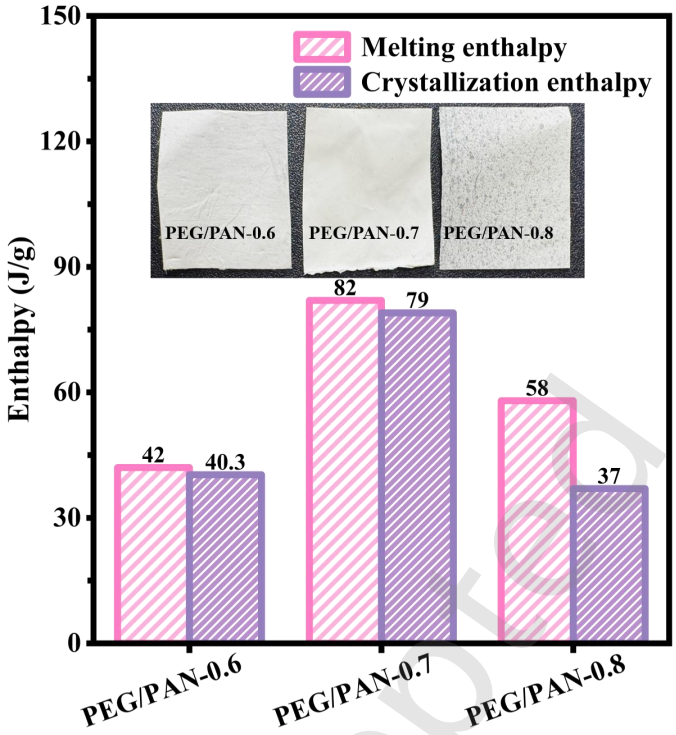


Figure S6 Enthalpies and photographs of PEG/PAN fiber membranes with varying PEG contents.

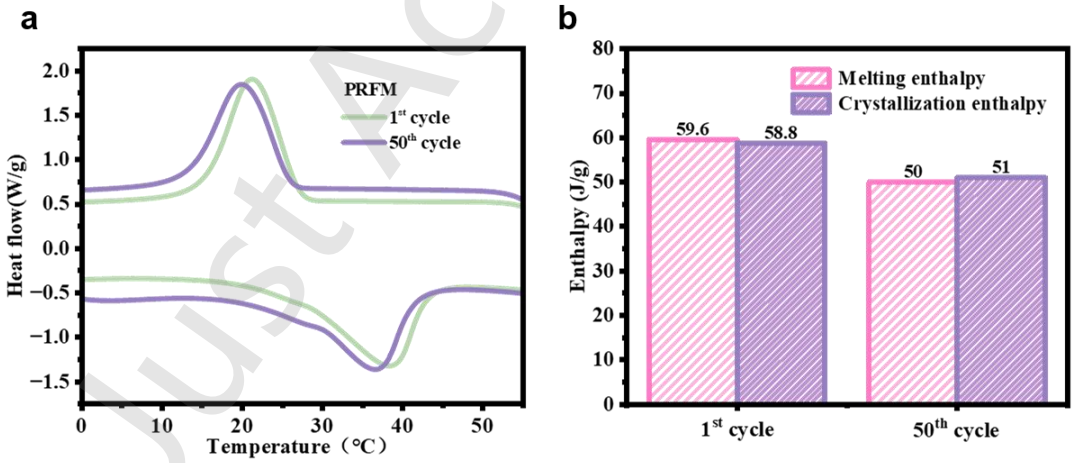


Figure S7 (a) DSC curves after the 50th melting-solidification cycle and (b) the corresponding melting and crystallization enthalpies.

Just Accepted

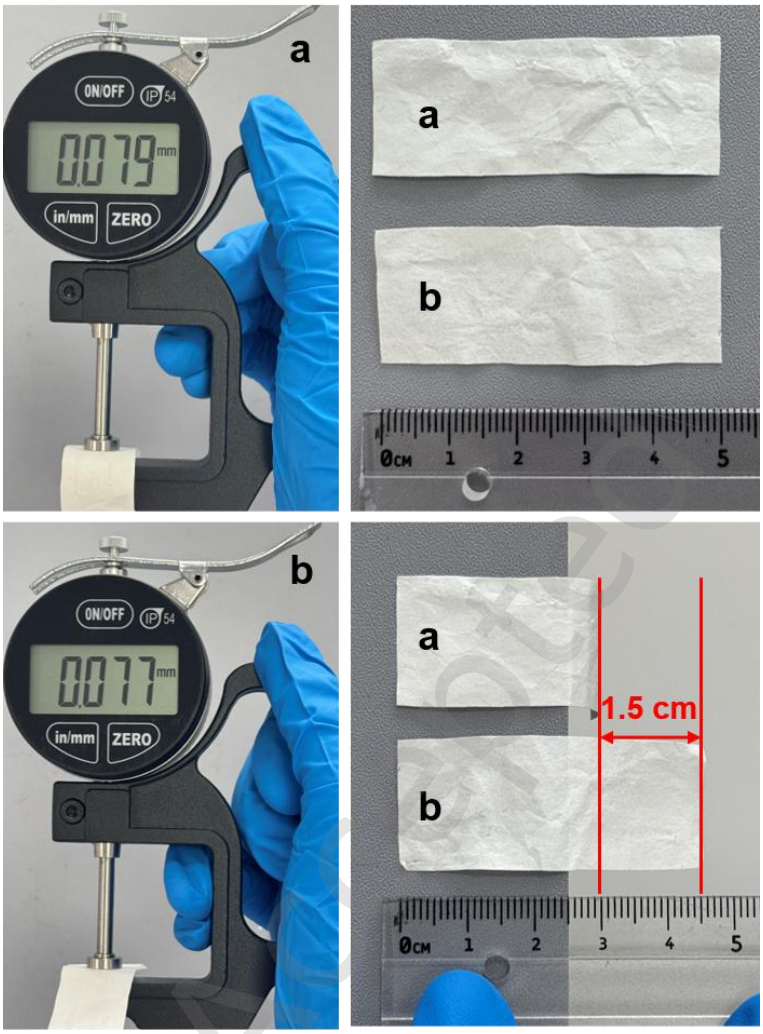
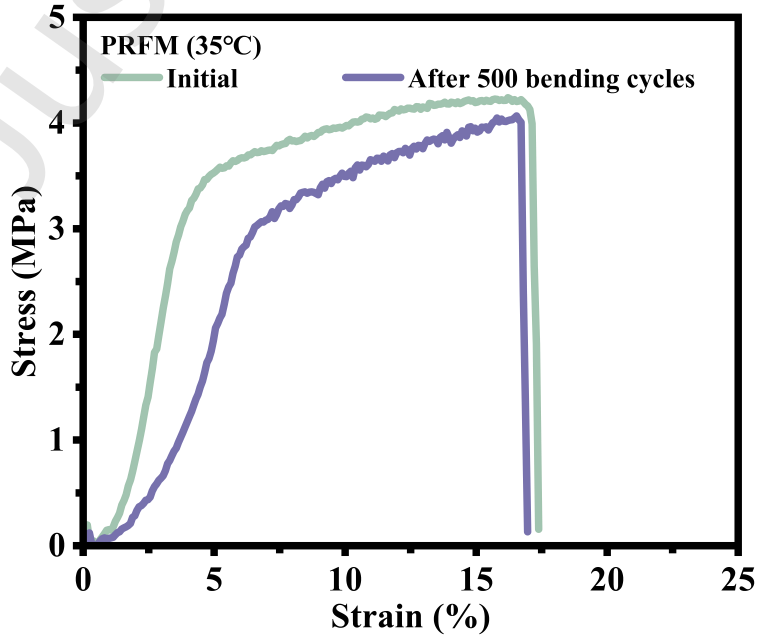


Figure S8 Draping tests of PEG/PAN-0.7 (a) after heating to 35 °C and (b) at room temperature (20 °C).



Just Accepted

Figure S9 Stress-strain curves of PRFM at 35 °C before and after 500 bending-recovery cycles.

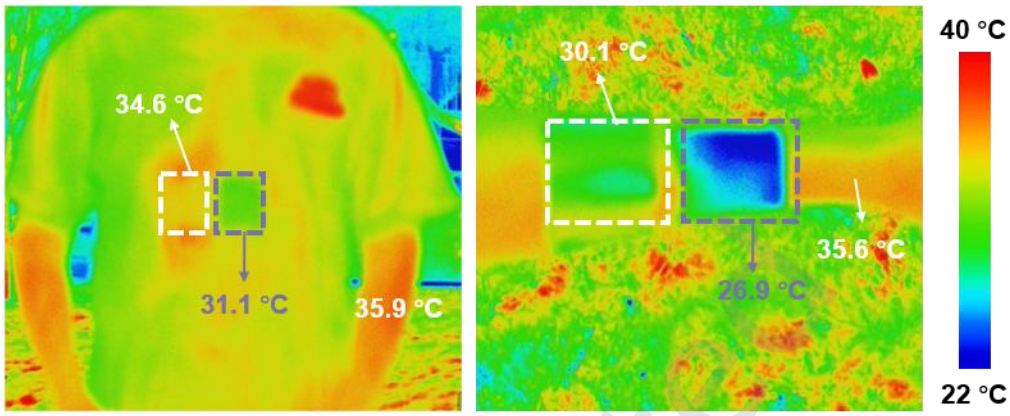


Figure S10 Infrared thermal thermograms of PRFM (right) and cotton (left) attached to a white cotton T- shirt and to the arm.



Figure S11 Photograph of the core suspension used for the preparation of PRFM.

Just Accepted

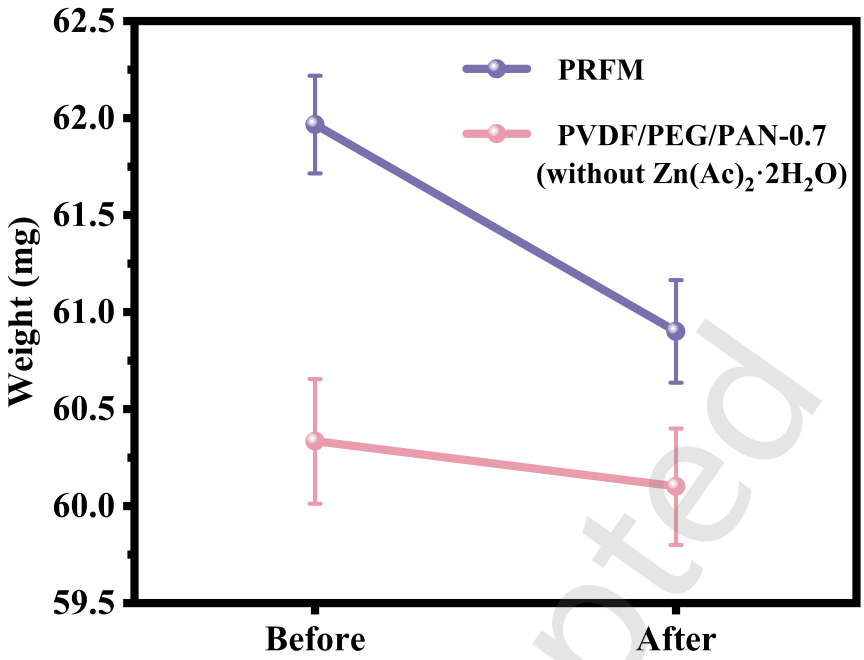


Fig. S12 Weight changes of PRFM and PVDF/PEG/PAN-0.7 (without $Zn(Ac)_2 \cdot 2H_2O$) before and after annealing.

Just Accepted